APPLICATION OF CELLULOSE BASED NANOMATERIALS IN 3D-PRINTED CEMENTITIOUS COMPOSITES

A Thesis
Submitted to
the Temple University Graduate Board

In Partial Fulfillment
of the Requirements for the Degree
MASTER OF SCIENCE

By
Abdullah Al Fahim
December 2023

Thesis Approvals:
Dr. Mehdi Khanzadeh Moradllo, Thesis Advisor, Department of Civil and Environmental Engineering
Dr. Joseph Thomas Coe, Department of Civil and Environmental Engineering
Dr. Yichuan Zhu, Department of Civil and Environmental Engineering

ABSTRACT

With the rapid development of concrete 3D printing for construction projects, it is crucial to produce sustainable 3D-printed cementitious composites that meet the required fresh and hardened properties. This study investigates the application of cellulose-based nanomaterials (CN) (i.e., abundant natural polymers) that can improve the mechanical properties of cement-based materials – in 3D-printed cementitious composites of ordinary portland cement (OPC) and alkali-activated materials (AAMs). A combination of low calcium fly ash and ground granulated blast-furnace slag was used as the precursor in AAM systems. This work examines the 3D-printed mixtures with varying binders and mixture proportions and with different dosages of cellulose-based nanomaterial known as cellulose nanocrystals (CNC) to optimize the formulation for the production of sustainable high-performance 3D-printed elements. A suite of experimental techniques was applied to study the impact of CNC on the fresh and hardened properties of the 3D-printed samples. The buildability of the alkali-activated mixtures was improved by increasing the CNC content, suggesting that the CNC performs as a viscosity-modifying agent in AAMs. The inclusion of CNCs up to 1.00% (by volume of the binder) improves the overall mechanical performance and reduces the porosity of 3D-printed OPC and heat-cured AAM samples. Further, the addition of CNC (up to 0.30%) in sealed-cured AAM samples improves their flexural strength due to the crack-bridging mechanism of CNCs. The addition of CNC densifies the microstructure of OPC samples by increasing the degree of hydration, however, no significant impact on the microstructure of AAMs is noticed. The OPC sample with CNC has approximately 25% increase in the degree of hydration at inner depths which can be attributed to the internal curing potential of CNC materials. The initial water absorption rate of heat-cured AAM samples is lower than the sealed-cured AAM samples and comparable to the OPC system. The developed printable “alkali-

activated-CNC" composites can provide an overall reduction in the environmental impacts of the 3D-printed cementitious composites by eliminating/reducing the need for different chemical admixtures to improve 3D-printed material consistency and stability, and replacing 100% of portland cement with fly ash and slag.

ACKNOWLEDGMENTS

I would like to express my sincere gratitude to all those who have contributed to the completion of this thesis. Their support, guidance, and encouragement have been invaluable throughout this research journey.

First and foremost, I am deeply grateful to my supervisor, Dr. Mehdi Khanzadeh Moradllo, for his unwavering support, invaluable guidance, and expertise. His insightful feedback, constructive criticism, and encouragement have been instrumental in shaping the direction and quality of this research. I am truly thankful for his mentorship and dedication. I would also like to acknowledge Temple University for providing the necessary resources, facilities, and support throughout the course of this research.

I would like to extend my heartfelt appreciation to the members of my thesis committee, Dr. Joseph Thomas Coe and Dr. Yichuan Zhu, for their time, expertise, and valuable input. Their insightful comments, suggestions, and constructive criticism have greatly enriched this work.

I want to express my heartfelt appreciation to all my family, friends, and loved ones who have supported me throughout this journey. Especially, I would like to acknowledge my deceased mother. She was not only my source of love and support but also a constant pillar of strength throughout my life. Her unwavering belief in me, her unconditional love, and her relentless encouragement have shaped the person I am today. In addition to that, I am deeply grateful to my wife, Najmun Nahar Keya, for her unconditional love, constant support, and understanding throughout this journey. Her belief in my abilities and encouragement have been a constant source of motivation. I love you!

I would like to thank my colleagues, Syed Jafar Shah Bukhari and Lynda Bouchelil, for their support, stimulating discussions, and encouragement during this research. Their friendship and presence have made this experience more enjoyable and meaningful.

Finally, I want to express my heartfelt appreciation to the United States Endowment for Forestry and Communities (through the P3Nano initiative) and the Pennsylvania Department of Community & Economic Development (through the Manufacturing PA Innovation Program) for providing the financial support for this study.

To all those who have supported me in various ways, I am truly grateful. This thesis would not have been possible without your invaluable contributions.

Thank you.

- *Abdullah Al Fahim*

TABLE OF CONTENTS

LIST OF TABLES

LIST OF FIGURES

GLOSSARY OF TERMS

2D	Two Dimensional
3D	Three Dimensional
AA	Alkali-Activated
AAM	Alkali-Activated Material
AASHTO	American Association of Highway and Transportation Officials
ACI	American Concrete Institute
activator/binder	Activator to Binder Ratio
AM	Additive Manufacturing
ASTM	American Society for Testing Materials
C-A-S-H	Calcium Aluminosilicate Hydrate
CMC	Carboxymethyl Cellulose
CN	Cellulose-based Nanomaterials
C-N-A-S-H	Calcium Sodium Aluminosilicate Hydrate
CNC	Cellulose Nanocrystals
CNF	Cellulose Nanofibers
DOH	Degree of Hydration
DTG	Derivative Thermogravimetry
EDX	Energy Dispersive X-ray
FA	Fly Ash
GGBFS	Ground Granulated Blast Furnace Slag
HRWR	High-Range Water-Reducer

HV	High Voltage
LFD	Large Field Detector
liquid/binder	Liquid to Binder Ratio
MoR	Modulus of Rupture
N-A-S-H	Sodium Aluminosilicate Hydrate
OPC	Ordinary Portland Cement
PE	Polyethylene
PP	Polypropylene
PVA	Polyvinyl Alcohol
RH	Relative Humidity
RPM	Revolutions Per Minute
SEM	scanning electron microscopy
TEM	Transmission Electron Microscope
TGA	Thermogravimetric Analysis
VMA	Viscosity-Modifying Admixture
w/c	Water to Cement Ratio
XRD	X-Ray Diffraction

CHAPTER 1
INTRODUCTION AND RESEARCH OBJECTIVES

3D printing has emerged as a promising technology in the construction industry for the fabrication of complex structures with intricate geometries [1]. In recent years, a growing interest has also been noticed in the use of cellulose-based nanomaterials (CNs) in construction materials, due to their potential to enhance the mechanical properties and durability of these materials [2]. This study aims to examine the feasibility and efficiency of incorporating CNs in 3D-printed cementitious composites. The study explores the potential of CNs to enhance the mechanical properties, durability, and sustainability of 3D printed cementitious composites. A suite of experimental techniques have been applied to evaluate the impact of CNs on the fresh and hardened properties of 3D-printed cementitious composites. The outcomes of this study can potentially contribute to the development of sustainable and high-performance construction materials with improved properties and reduced environmental impact.

This study investigates the use of a type of cellulose nanomaterial known as cellulose nanocrystals (CNC) in 3D-printed alkali-activated fly ash/slag mixtures; a new class of alternative cementitious materials that replaces 100% of portland cement with fly ash (a byproduct of the coal combustion process) and slag (a by-product of iron in blast-furnace). Replacing all conventional concrete with alkali-activated mixtures will likely result in up to 80% less CO_2 emission than OPC production, depending on the precursor type and alkali activator sources [3, 4]. In addition, the effect of CNC incorporation on fresh properties of alkali-activated mixtures are investigated. The main objectives of this study are:

- Developing sustainable 3D printable alkali-activated composites with and without cellulose nanocrystals (CNC)
- Determining the optimum dosage of CNC in 3D printed composites
- Investigating the viability of using CNC as a potential viscosity-modifying additive in 3D printing of OPC and AA systems
- Examining the fresh properties (extrudability and buildability), hardened properties (compressive strength, flexural strength, porosity, and bulk electrical resistivity), and microstructure (using thermogravimetric analysis (TGA), scanning electron microscopy (SEM), and x-ray diffraction (XRD)) of 3D-printed “alkali-activated-CNC” with “OPC-CNC” composites
- Identifying the potential applications and benefits of using CNCs in 3D printing of cementitious composites for sustainable construction.

CHAPTER 2
LITERATURE REVIEW

2.1 Additive Manufacturing

Additive manufacturing (AM), commonly known as three-dimensional (3D) printing is an automated layer-by-layer production process and has seen rapid development in construction industry in the past decade [5, 6]. When compared to conventional construction processes, 3D concrete printing technology has the potential to increase customization, optimize construction time, and reduces manpower, work-related injuries and overall cost in construction projects [6-8]. 3D concrete printing involves repetition of a predesigned 2D element on top of each other to create a 3D model [7]. 3D printing of concrete is mainly classified into three main categories: material extrusion, material jetting, and particle-bed binding. Among them, extrusion-based 3D concrete printing which employs a continuous filament extrusion and a layer-wise process for forming objects without formwork is widely used due to its potential to be applied in large-scale on-site construction [9]. However, important challenges exist for cost-effective and sustainable 3D printed cementitious mixtures that meet the required fresh and hardened properties. In previous studies, higher cement content and various chemical and mineral admixtures are primarily employed to meet the design needs of 3D-printed cementitious composites such as high workability of the mixture during extrusion, longer open time to allow interlayering bond formation and development of early strength to support subsequent layer loading [10, 11]. These combinations of materials lead to less cost-effective and high carbon footprint 3D printing mixtures for application in the building industry. For instance, portland cement is one of the primary sources of global warming and accounts for approximately 8% of worldwide CO_2 emissions [12]. Therefore, it is crucial to

find alternative cementitious materials and additives to produce sustainable 3D-printed cementitious composites.

2.2 Cellulose Nanomaterials

Cellulose-based nanomaterials (CN) such as Cellulose Nanocrystals (CNCs) and Cellulose Nanofibers (CNFs) can serve as an alternative additive to improve the fresh and hardened properties of 3D-printed cementitious composites [2, 13, 14]. Cellulose nanocrystals (CNC) are the crystalline part of these polymers and Cellulose nanofibers (CNFs) are naturally synthesized nanofibers usually extracted from trees and plants [15, 16]. CNCs are typically 0.05 – 0.5 μm long and have a width of 3 – 5 nm [17]. On the other hand, CNFs are about 1–5 μm long and 5–50 nm wide [16]. The Transmission Electron Microscope (TEM) images of CNC and CNF in aqueous suspension are shown in Figure 1 [18, 19]. CNs are a promising material for nanoscale reinforcing due to their high aspect ratio, high elastic modulus, high strength, low density, and reactive surfaces that can be functionalized. Additionally, they are renewable, biodegradable, sustainable, low cost, and present in high abundance in nature. Furthermore, the extraction processes of these nanomaterials have low environmental and safety risks compared to other conventional nano-reinforcing materials [15, 17]. The application of CNs is gradually increasing in concrete technology [20]. In previous studies, CN-incorporated cement pastes showed an improvement in mechanical performance of the cement pastes by improving the degree of hydration [15, 20, 21]. Additionally, depending on the dosage, CNs have the capability to alter the fresh properties of cement pastes [21, 22]. On the other hand, in 3D concrete printing, CN inclusion can decrease the extrusion pressure (i.e., improves the extrudability of cementitious mixture), and can increase the degree of hydration and flexural strength of the 3D printed cementitious samples [11]. However, previous research investigated limited mixtures with a higher content of ordinary portland cement

(OPC: ≈80% of the total weight of composite). These mixtures are neither cost-effective nor sustainable.

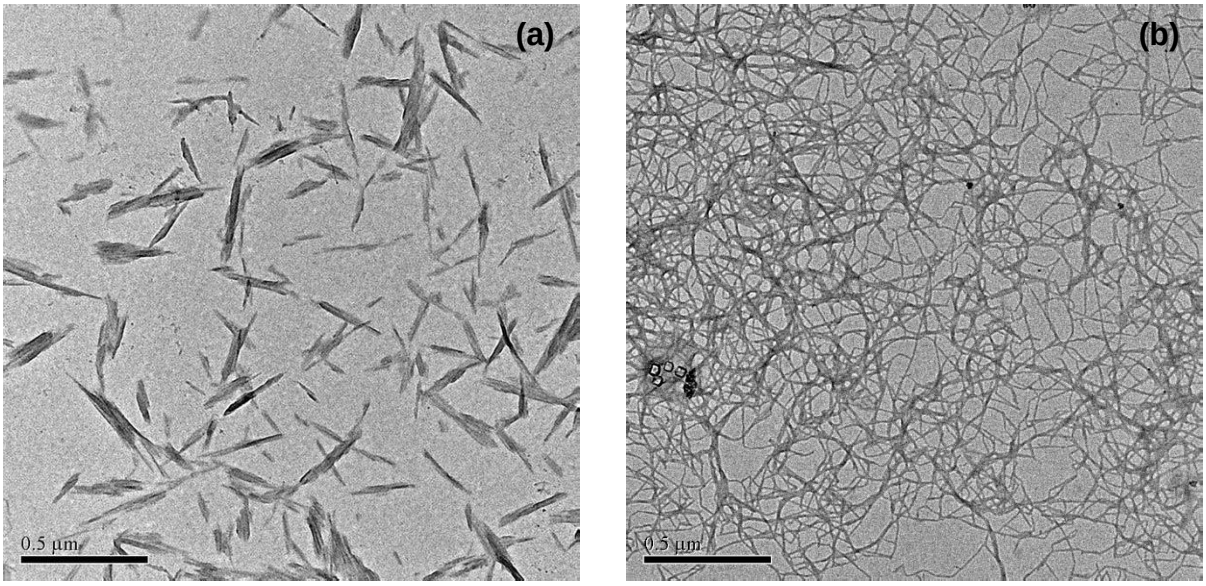

Cellulose nanocrystals (CNC) Cellulose nanofibers (CNF)

Figure 1. Transmission Electron Microscope images of (a) CNC and (b) CNF

2.3 Alkali-activated Materials

Alkali-activated materials (AAMs) are manufactured by a chemical reaction that takes place between an alkaline activator and reactive aluminosilicate materials [23]. AAMs can be generated from a range of widely available aluminosilicate precursors such as blast furnace slag, coal fly ash, metakaolin, and ground waste glasses, having differing availability, reactivity, cost, and significance worldwide [23-25]. Fly ash primarily create a three-dimensional alkaline aluminosilicate hydrate known as sodium aluminosilicate hydrate (N-A-S-H) gel [26] and calcium rich precursor such as slag facilitates the formation of calcium aluminosilicate hydrate (C-A-S-H) gel [27]. The N-A-S-H and C-A-S-H can coexist or formulate a hybrid gel known as calcium sodium aluminosilicate hydrate (C-N-A-S-H) gel in AAM system depending on the relative ratio

of slag and fly ash in an AAM system [27, 28]. Due to their ceramic-like nature, AAMs have relatively low flexural strength which results in brittle failure [29]. To overcome this issue, the addition of natural and synthetic fibers to the matrix of AAMs has been investigated. It has been shown that the flexural strength of AAM can be increased up to 450% depending on the type of fiber [29]. In 3D printing of AAMs, employing fly ash and slag as the primary raw material is highly desirable to eliminate their global storage difficulties in landfills [4]. The effect of different slag/fly ash ratios (1.00, 0.75, 0.50, and 0.25) on the mechanical anisotropy of 3D printed AAMs has been investigated [30]. Different clay-based minerals such as attapulgite, magnesium alumino silicate, hydrophilic bentonite, and calcined halloysite clay have been used as additives to tailor the fresh properties of 3D printable AAMs [31-33]. In addition to the additives, the alkaline activator used in 3D printing of AAMs also helps to reduce the yield stress and improves the cohesiveness of the fresh mixtures [34]. The inclusion of polyvinyl alcohol (PVA) [35], polypropylene (PP) [6], and polyethylene (PE) [36] fibers has shown increased flexural strength of 3D printed AAMs due to the crack-bridging mechanism of these fibers. However, there is a lack of research on the 3D printability of CN incorporated AAMs.

CHAPTER 3
RESEARCH SIGNIFICANCE

The application of cellulose-based nanomaterials in 3D printing of cementitious composites holds significant research significance. CNs have high tensile strength, modulus, and aspect ratio which results in increased strength, toughness, and durability of 3D-printed cementitious composites. This enhanced mechanical performance can lead to the development of more reliable and structurally sound construction materials. In addition to that, cellulose-based nanomaterials are derived from renewable sources, such as plant fibers, making them an environmentally friendly choice. Alkali-activated materials are considered environmentally friendly as they utilize industrial by-products. Alkali-activated materials has the potential to divert waste materials from landfills and reduce the reliance on traditional cement production. Additionally, the production of alkali-activated materials generates lower greenhouse gas emissions compared to traditional cement manufacturing and promotes sustainability in construction. By utilizing these materials in 3D-printed cementitious composites, it is possible to reduce the dependence on non-renewable resources and decrease the carbon footprint associated with traditional construction methods. Moreover, the rheological properties of cementitious materials play a crucial role in 3D printing. Cellulose-based nanomaterials can improve the rheology of cementitious composites by enhancing their flowability, reducing sedimentation, and preventing segregation during the printing process. Understanding the influence of cellulose nanomaterials on the printability of 3D-printed cementitious composites is vital for optimizing the printing parameters and achieving accurate and reliable printed structures.

The application of cellulose-based nanomaterials in 3D-printed cementitious composites offers a wide range of benefits, including improved mechanical properties, sustainability, and enhanced

rheology. Investigating and optimizing the use of these materials in 3D printing can significantly contribute to the advancement of construction technology and the development of high-performance and eco-friendly building materials.

CHAPTER 4

MATERIALS AND MIXTURE PREPARATION

4.1 Materials

A Type I ordinary portland cement (OPC) conforming to ASTM C150 with a specific gravity of 3.15 was used in this study. Class F fly ash (FA) conforming to ASTM C618 with a specific gravity of 2.42 and ground granulated blast furnace slag (GGBFS) conforming to ASTM C989 with a specific gravity of 2.84 was implemented as precursors for preparing alkali-activated (AA) mixtures. The chemical compositions of cementitious materials are reported in Table 1.

Table 1
Chemical compositions and physical properties of cementitious materials.

Component	Mass (%)		
	OPC	FA	GGBFS
SiO_2	19.59	51.81	31.72
Al_2O_3	4.66	27.19	13.29
Fe_2O_3	2.78	12.09	-
CaO	63.30	2.64	41.4
MgO	3.45	0.85	8.35
SO_3	3.16	0.81	1.80
Na_2O	0.33	0.22	-
K_2O	0.95	2.39	-
TiO_2	0.22	-	-
Na_2O_{eq}	0.96	1.79	0.77
LOI	1.27	2.96	1.67

For OPC systems, a liquid viscosity-modifying admixture (VMA) with a chemical composition of 2-phenylphenol (ISO)biphenyl-2-ol; 2- hydroxybiphenyl and a polycarboxylate-based high-range water-reducing admixture (HRWR) was used to achieve extrudable and buildable mixtures. For AA mixtures, sodium carboxymethyl cellulose (CMC) in powder form was used as a viscosity-modifying admixture. In addition, a sodium-based activator composed of 5.0 M Sodium Hydroxide (NaOH) and N Grade Sodium Silicate (Na_2SiO_3) was used as an alkali activator. The 5.0 M NaOH solution was prepared using NaOH pellets of 97% purity and deionized water. A commercially available N grade Na_2SiO_3 solution with a concentration of 37% (28% silica and 9% sodium oxide) and a specific gravity of 1.39 was used. The cellulose nanocrystals (CNC) are in aqueous suspension with 10.6% solids. The CNC was acquired from the University of Maine-Process Development Center for use in both OPC and AA mixtures. The CNCs are approximately 5-20 nm wide and 150-200 nm long [37]. The dry density of CNCs is 1.5 g/cm^3 and the bulk density of the aqueous gel is 1.0 g/cm^3.

4.2 Mixture Design

Four different cementitious paste mixtures using Type I OPC with varying water-to-cement ratios (w/c=0.26-0.315) and dosages of CNC materials (0.0-1.75% by volume of cementitious materials) were prepared, as listed in Table 2. Additionally, four alkali-activated FA/GGBFS mixtures with varying dosages of CNC were prepared, as listed in Table 3. A range of liquid (activator+water)-to-binder ratios (0.32-0.345) was examined to produce extrudable and buildable AA mixtures. The AA precursor consists of 70% FA and 30% GGBFS by mass. In Table 2 and Table 3, the control systems were prepared without the addition of CNC in the mixture. For the mixtures with a high dosage of CNC (≥1%), the water-to-cement ratio, liquid (activator+water)-to-binder ratio, VMA, CMC and HRWR dosages were adjusted to make the mixture extrudable, printable and buildable.

Table 2
Mixture proportions of 3D printable OPC composites with/without CNC.

Mixture ID	Cement (g)	w/c	Water (g)	CNCs slurry (g)	VMA (g)	HRWR (g)	CNCs/cement (vol%)
OPC–Control	1200	0.26	312.00	0	21.60	9.84	0.00
OPC–0.25% CNC	1200	0.26	299.95	13.48	21.60	9.84	0.25
OPC–1.00% CNC	1200	0.26	263.81	53.91	14.40	12.00	1.00
OPC–1.75% CNC	1200	0.315	293.66	94.34	38.40	11.40	1.75

Table 3
Mixture proportions of 3D printable AA composites with/without CNC.

Mixture ID	FA (g)	GGBFS (g)	Liquid /binder	NaOH (g)	Na_2SiO_3 (g)	CNCs slurry (g)	CMC (g)	CNCs/binder (vol%)
AA–Control	840	360	0.32	326.40	57.60	0.00	6.00	0.00
AA–0.30% CNC	840	360	0.32	311.22	54.92	19.98	0	0.30
AA–1.00% CNC	840	360	0.335	291.10	51.37	66.59	0	1.00
AA–1.50% CNC	840	360	0.345	275.99	48.70	99.89	0	1.50

4.3 Mixture Process

For preparing the OPC mixtures, the CNC was mixed with water and admixtures using a vacuum mixer at 450 RPM for 1.5 minutes for proper dispersion of the CNC in the solution. In the case of AA mixtures, activator solution and CNC materials were mixed in a vacuum mixer at 450 RPM for 1.5 minutes. As stated, a sodium-based activator composed of 5.0 M NaOH and N Grade Na_2SiO_3 in an 85:15 mass ratio was utilized. This ratio was selected based on preliminary trials to

produce extrudable and buildable AA systems. The prepared CNC solutions were added to cement or AA precursors and the following procedure was used for mixing the materials: (i) mix at slow speed (104 RPM) for 1.5 minutes using a bench scale mortar mixer; (ii) stop the mixer for 15 seconds and scrape down the materials from bowl sides; (iii) mix at medium speed (194 RPM) for 1.5 minutes; and (iv) transfer the material to the vacuum mixer and mix at high speed (300 RPM) for another 3 minutes to improve CNC dispersion and minimize entrapped air content. The mixing procedure for the OPC and AA systems with/without CNC is shown in Figure 2.

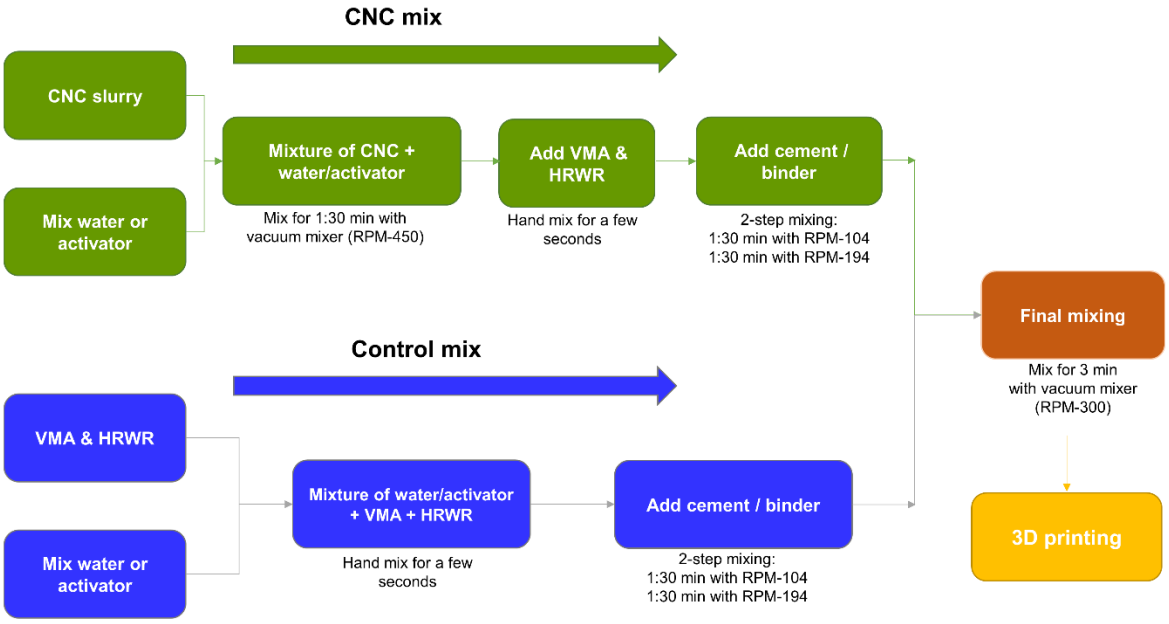

Figure 2. Mixing procedure for OPC and AA mixtures with and without CNC.

4.4 Printing Setup

This study implements an extrusion-based 3D Printer which is developed for printing clay elements. This printer was modified to accommodate the 3D printing of cementitious composites with CNs. First, to minimize the material loading and unloading time into the printer, a drill motor

was added to the printer assembly to automatically retract the ram and screw without the need to unclamp the cartridge extrusion assembly. Additionally, the cartridge assembly was separated into two pieces. Section A, which is permanently attached to both the gantry and extrusion motor, and section B, where material can be easily loaded onto and consolidated to remove entrapped air voids (Figure 3). These modifications helped to increase the print open time and improve the extruded material consistency.

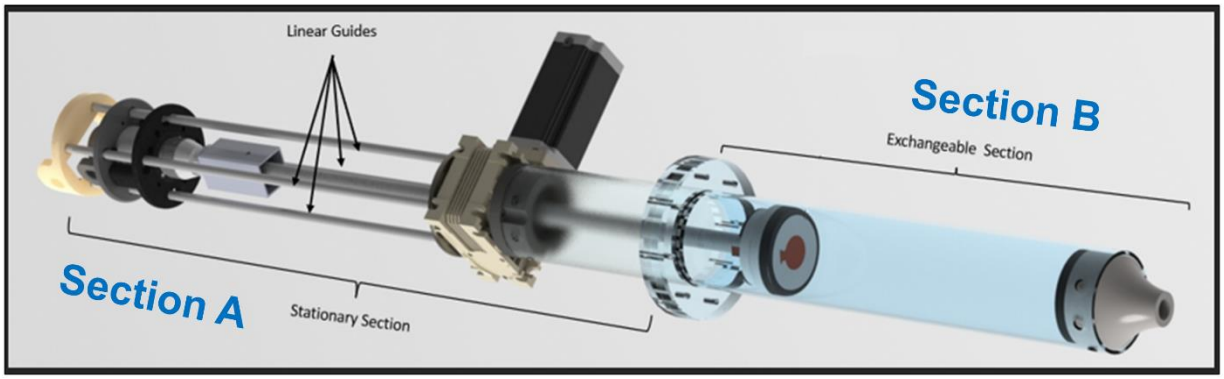

Figure 3. The extrusion-based 3D Printer with two separated sections of the cartridge assembly.

4.5 Sample Preparation

Ultimaker Cura was used to develop the 3D printing model. A prismatic beam model with a layer height of 5 mm is developed for printing. The geometry of the prismatic samples is 50(Height) × 50(Width) × 178(Length) mm^3 having 11 layers. The perimeter filament of the specimens is printed in a straight-line pattern and the infill filaments are printed in a zigzag pattern (Figure 4). The printing speed for the perimeter filament is 5 mm/s and it is increased to 10 mm/s for the infill filaments. The travel speed of the printer is 40 mm/s. The width of the perimeter filament is 4 mm and it is changed to 3.5 mm for the infill filaments.

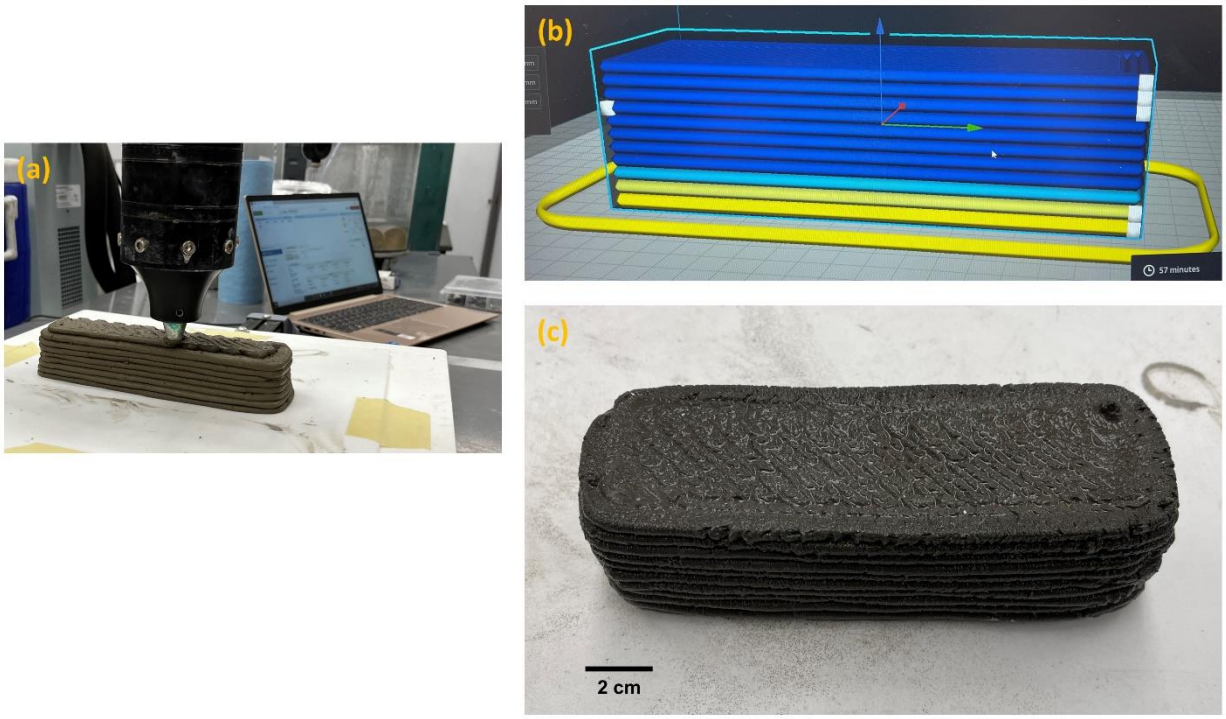

Figure 4. (a) Extrusion of the cementitious composites, (b) 3D model of prismatic beam samples, and (c) 3D printed prismatic beam for testing.

4.6 Curing

The printed OPC samples were wet-cured at 23 °C until testing (28 days). The AA samples were cured in a sealed environment at 23 °C for 28 days. Additionally, a set of AA samples was heat-cured. The heat-cured samples were placed in a sealed container to minimize moisture loss and placed in an oven at 60 °C for 7 days.

CHAPTER 5
EXPERIMENTAL TESTING

A suite of experimental techniques was applied to study the impact of CNCs on the fresh and hardened properties of the 3D-printed samples. This includes:

- Mechanical Performance:
    - Compressive Strength
    - Flexural Strength
- Mass Transport Properties:
    - Porosity
    - Water Absorption
    - Bulk Electrical Resistivity
- Microstructure Analysis:
    - Thermogravimetric Analysis
    - Scanning Electron Microscopy and Energy-dispersive X-ray Spectroscopy
    - X-ray Diffraction

These experimental techniques are discussed in detail from Section 5.1 to Section 5.7.

5.1 Compressive Strength

After curing, the printed prisms were sawn using a wet saw to prepare 25×25×25 mm^3 cubic samples to measure their compressive strength. The Tinius Olsen 300K Super L compression test system was used to test the cubic samples. Two compression platens were used on the top and bottom parts of the samples to evenly distribute the compression loads during the test. The cubic samples were tested at the rate of 680 kg per min (≈1500 pounds per min) till the sample failed

(i.e., extensively cracked). The recorded peak (failure) load was divided by the cross-sectional area resisting the load to calculate the compressive strength of the sample. Seven samples were tested per mixture and the average value was reported in units of megapascals (MPa).

5.2 Flexural Strength

After curing, the printed prisms were cut using a wet saw to prepare 25×25×152 mm^3 rectangular samples to determine their flexural strength (i.e., modulus of rupture; MoR). MoR is a measure of the tensile strength of the 3D printed samples. The Tinius Olsen H5KT Benchtop Tester was used to test the samples (Figure 5). All specimens were tested in a center-point bending test setup with a span of 127 mm (5 in.) under displacement control at the rate of 1.0 mm/min, and the peak (failure) load was recorded. The MoR was calculated based on Equation 2 of ASTM C293-16. Three samples were tested per mixture and the average value was reported in units of megapascals (MPa).

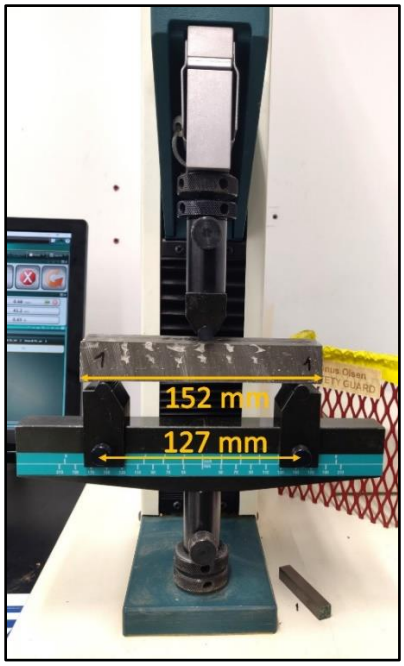

Figure 5. The flexural strength test setup with a rectangular sample under center-point bending.

5.3 Porosity

After curing, the printed prisms will be sawn to prepare 25×25×25 mm^3 cubic samples. The cubic samples were tested to determine their permeable pores, following ASTM C642-21 (with the exception that the samples were saturated by vacuum, instead of being placed into boiling water) [38]. After the samples are oven-dried at 105 ± 2 °C for approximately 3 days (until the weight of the samples stabilized), the mass was measured and then they were placed into the vacuum chamber with a vacuum level of 933 ± 266 Pa for 3 hours. Lime water (i.e., saturated CaOH solution) was drawn into the vacuum chamber, and samples were maintained under vacuum for another hour. The samples were kept submerged for an additional 20 hours after the vacuum session. The mass of the saturated surface-dry samples and their apparent mass under water were measured to calculate the porosity according to ASTM C642-21.

5.4 Bulk Electrical Resistivity

The bulk electrical resistivity of saturated samples was measured after porosity testing. Electrical resistivity is a fundamental property of a cementitious material that indirectly measures the resistance of microstructure against fluid penetration. The electrical resistance of the cubic samples was measured using a Resistivity Meter with a frequency of 1 kHz at 23 ± 2 °C. Two 102 mm in diameter stainless steel plate electrodes were used with two pieces of sponge with a thickness of 3 mm. During the test, the sponge were saturated with lime water and placed between specimens and plate electrodes to ensure electrical connection. The electrical resistivity was calculated using the measured electrical resistance minus the resistance of two pieces of sponge according to AASHTO TP 119.

5.5 Water Absorption

For the absorption test, OPC – 1.00% CNC 28-day wet cured, and AA – 1.00% CNC both 28-day sealed cured and 7-day heat-cured samples were selected. After curing, the printed prisms were sawn to prepare 25×25×25 mm^3 cubic samples similar to the porosity test. The cubic samples were tested to determine their initial absorption rate, following ASTM C1585 – 20 (with the exception that the samples were oven-dried, instead of having 50% RH). The samples were oven-dried at 105 ± 2 ℃ for approximately 3 days until the weight of the samples stabilized. After the drying period, the side surfaces of the samples were sealed with aluminum tape to avoid evaporation from the sample during testing and to simulate one-dimensional absorption. The bottom surface of the samples was exposed to water and the water level was maintained 1 to 3 mm above the bottom of the sample during the absorption test. Three samples were tested for each mixture.

5.6 Thermogravimetric Analysis (TGA)

Thermogravimetric analysis (TGA) was implemented to investigate the amount of chemically bound water from hydration products and dehydroxylation of alkali aluminosilicate gels in OPC and AA samples. The chemically bound water and hydroxyl ions are indications of the degree of hydration (DOH) of OPC samples and the degree of reaction of AA samples, respectively. For bulk TGA, approximately a 10×10×20 mm^3 thick slice was cut from the center of prismatic printed samples. For TGA profiles over the depth, a 10 mm thick slice was cut from the middle of the samples perpendicular to the length. The slice was then cut into 4 segments along the height. These slices are then grounded into fine powder using a laboratory ball mill grinder and sieved (<75 μm) to avoid the inclusion of large particles. The powder was then placed in an oven at 105 ℃ for approximately 24 hours. Approximately 40 mg of material was taken from the powdered sample and TGA was performed to determine the amount of chemically bound water and hydroxyls. The

analysis is performed by placing the powdered sample into a platinum crucible and heating it from room temperature to 50 °C, at a rate of 20 °C/minute under a constant stream of nitrogen gas. The temperature is then held constant for 10 minutes. Later the sample is heated from 50 °C to 850 °C at a rate of 20 °C/min in a nitrogen-purged atmosphere. The total amount of chemically bound water and hydroxyls in OPC and AA samples is estimated by analyzing TGA and derivative thermogravimetry (DTG) curves using the modified tangential method; calculated as the difference between the 50 °C and 580 °C (onset of CO_2 decomposition) mass loss measurements.

5.7 Scanning Electron Microscopy (SEM) and Energy Dispersive X-Ray Spectroscopy (EDX)

Quanta 450 FEG scanning electron microscope was utilized to image the microstructure of the AA samples. For SEM imaging, AA – Control and AA – 1.00% CNC both 28-day sealed cured and 7-day heat-cured samples were selected. A 5×5×5 mm^3 sample was taken from the core of the prismatic specimens after flexural testing. A High Voltage (HV) electron beam with an intensity of 20 kV was employed for imaging the fractured surfaces using the Large Field Detector (LFD; i.e., secondary electron imaging). Energy dispersive X-ray (EDX) was performed to analyze the chemical composition of reaction products.

5.8 X-Ray Diffraction (XRD)

X-ray diffraction was performed on powdered samples obtained from the core of AA samples. Crystalline phases present in the samples were identified using Bruker AXS D8 Advance X-ray diffractometer equipped with Cu-Kα radiation having a wavelength of 0.15418 nm. AA – Control and AA – 1.00% CNC both 28-day sealed cured and 7-day heat-cured samples were selected for XRD. A 10×10×20 mm^3 thick slice was cut from the center of prismatic printed samples and was

ground into fine powder using a laboratory ball mill grinder. The scan range of the spectrum was from 5º to 55º with an increment of 0.02045º in 2θ angle.

CHAPTER 6
RESULTS AND DISCUSSION

6.1 Acceptance Criteria for Printable Mixtures

The OPC and AA mixtures for different testing on hardened samples were screened and selected based on the extrudability and buildability criteria. This section discusses these criteria in detail.

Extrudability – The extrudability of the mixtures was examined based on the consistency of the extruded filaments. A successful print should have consistent layering and there should be no splitting or tearing of the filament. Several parameters such as admixture content and "w/c" or "activator/binder" were varied to design extrudable mixtures with optimum material content. After designing control mixtures (i.e., without CNC), different dosages of CNC were added to the control mixtures. To design extrudable CNC mixtures, the admixture content (HRWR and VMA contents) and "w/c" in OPC systems and "activator/binder", activator composition, and precursor composition ("FA/GGBFS") in AA systems were varied. For instance, the required "liquid/binder" was higher in AA mixtures compared to OPC mixtures and increased linearly as a function of CNC dosage to produce extrudable mixtures, as shown in Figure 6. However, OPC mixtures required a more dramatic increase of "liquid/binder" above 1.00% CNC concentration (by volume of binder) in order to be extrduable (Figure 6). This can be attributed to the dispersion quality of CNC (i.e., agglomeration of CNC) in different systems. It seems that the 1.00% CNC dosage is the critical concentration for CNC agglomeration in the studied OPC mixtures.

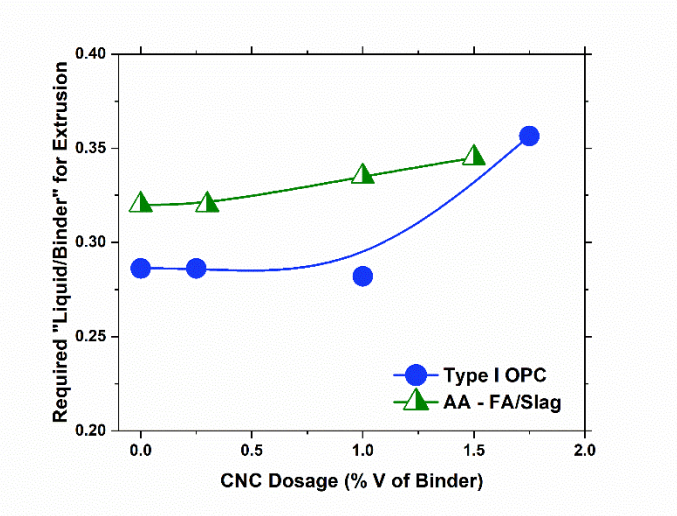

Figure 6. Required "liquid/binder" as a function of CNC dosage for successful extrusion of OPC and AA mixtures.

Buildability – The buildability of the mixtures was examined based on the ability of the printed mixture to retain its shape and bear the overburdened weight of the successive layers during printing. A buildable mixture should also have the ability to bond with the previous layer. The buildability of mixtures is investigated using the number of successfully stacked layers before failure (e.g., 11 layers) or excessive water leak (i.e., open print time). The number of stacked layers is an indication of the stability (i.e., the effective stiffness) of the print material. The excessive water leak is an indication of the inconsistency of the mixture over the course of the print due to the setting or segregation of material under constant extrusion pressure [39, 40]. The buildability of the mixtures was improved by increasing the dosage of VMA in OPC mixtures or CNC/CMC in AA mixtures because it increases the shape retention properties of the filaments. For example. the AA mixture without the addition of either CMC or CNC was not buildable. It seems that the CNC performs as a VMA in AA mixtures.

Based on these extrudability and buildability criteria, the optimum printable mixtures were selected for further testing. For example, Figure 7 shows the printable/not-printable regions for AA systems as a function of activator and precursor compositions. The AA mixture with a "$NaOH/Na_2SiO_3$" mass ratio of 85:15 and a "FA/GGBFS" mass ratio of 70:30 was selected as the optimum AA mixture for printing, as shown in Figure 7. In several AA mixtures, sucrose was used as a retarder to increase the open print time by extending the setting time. However, these mixtures were not selected for further testing due to their low strength properties. Other chemical and mineral admixtures such as accelerators can be implemented to improve the extrudability and buildability of the mixtures. However, testing these admixtures was not the focus of this study.

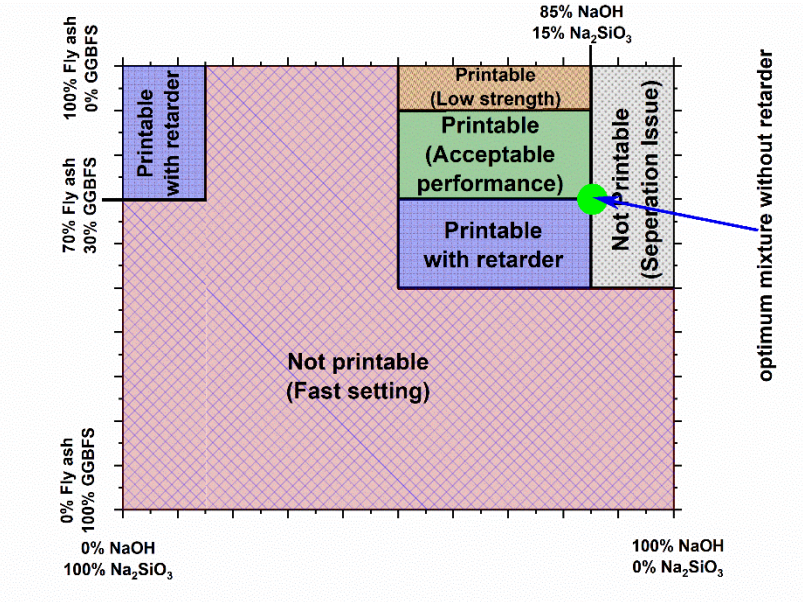

Figure 7. "Fly ash/GGBFS" versus "$NaOH/Na_2SiO_3$" to determine regions of printable mixtures and optimum mixture design for AA systems.

6.2 Mechanical Performance of 3D Printed OPC and AA Mixtures

Figure 8 shows the calculated compressive strength and MoR of the 3D printed OPC and AA samples as a function of CNC content. Based on Figure 8, the addition of CNC by 0.25-1.00%

increases the compressive strength and MoR of OPC samples by 8-15% when compared to control samples. However, the compressive strength and MoR of OPC samples diminish when the CNC dosage was increased above 1.00%. This can be attributed to the agglomeration of CNCs (i.e., their dispersion quality), as well as the increase in the "liquid/binder" of mixtures with high dosages of CNCs (to produce printable mixtures). The agglomeration regions can act as weak points in the microstructure of cementitious systems, and consequently reduce the mechanical performance of the 3D printed samples [17]. It seems that the 1.00% CNC dosage is the critical concentration for CNC agglomeration in the studied mixtures.

The AA mixtures behave differently than OPC systems. While the sealed cured AA samples have a lower compressive strength compared to OPC systems, the addition of higher CNC dosages further lowers the compressive strength. However, their MoR values are comparable to OPC samples for the addition of CNC by up to 0.30% and it diminishes when the CNC dosage was increased above 0.30%. The lower compressive strength of sealed cured AA samples can be due to their higher "liquid/binder" when compared to that of OPC samples. Additionally, AA systems with low calcium FA (i.e., Class F FA) show a slow strength development [41]. For the heat-cured AA samples, both compressive strength and MoR were increased compared to the sealed-cured AA samples. In addition, the inclusion of CNC increased both the compressive strength and MoR of heat-cured AA samples. The heat curing can accelerate the dissolution of FA and GGBFS particles (i.e., increases the reactivity), and hence improves the microstructure of AA systems [42]. This has been discussed in detail in Section 6.6.

Figure 9 presents the MoR values as a function of the compressive strength of different mixtures, and the comparison with the developed relationships based on ACI 318-19 and ACI PRC-363-10

documents. The majority of the obtained values from printed samples lie between two developed ACI relationships. It is interesting that the heat-cured AA samples exceed the ACI PRC-363-10 curve due to high MoR (i.e., high ductility).

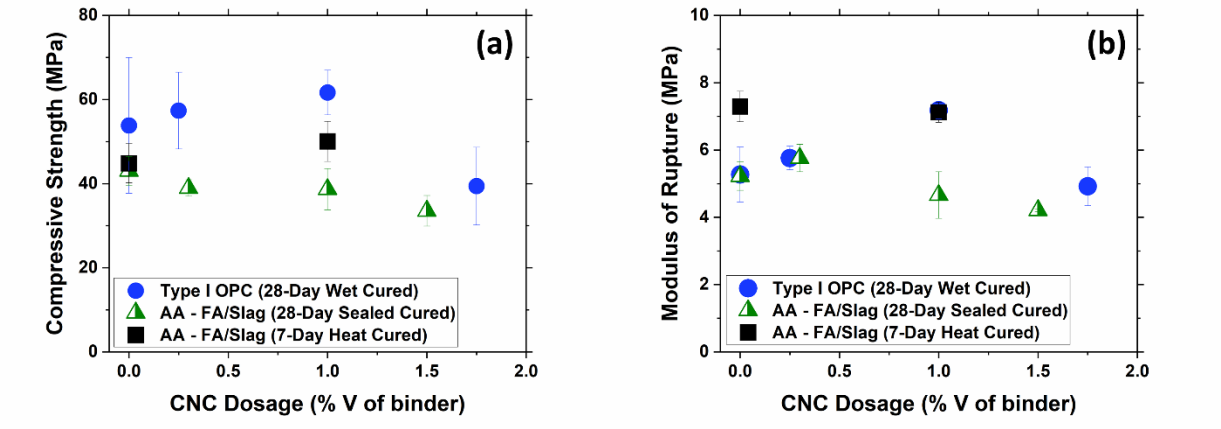

Figure 8. (a) Compressive strength and (b) modulus of rupture of 3D printed OPC and AA samples with different dosages of CNC materials.

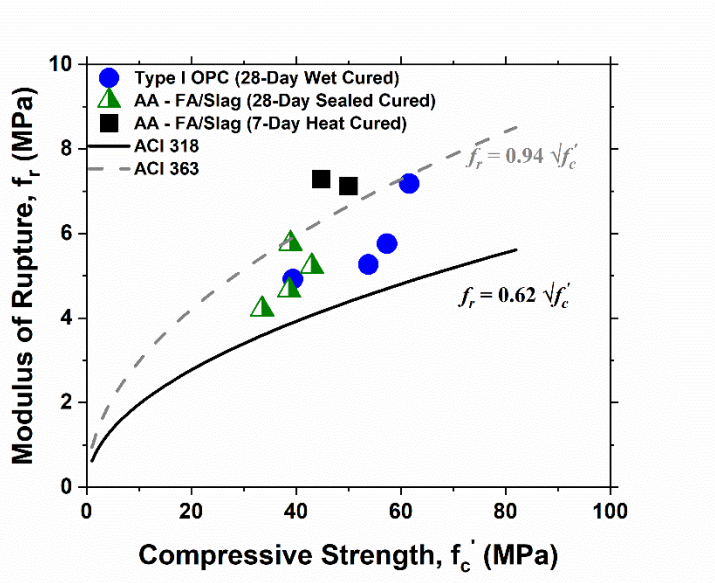

Figure 9. Modulus of rupture as a function of compressive strength for 3D printed OPC and AA samples with different dosages of CNC materials, and the comparison with ACI 318 and 363 equations.

6.3 Porosity, Electrical Resistivity, and Absorption of 3D Printed OPC and AA Mixtures

Figure 10a shows the measured porosity of the 3D printed OPC and AA samples as a function of CNC content. The porosity of printed samples decreases with the addition of 0.25-1.00% CNC. However, there is an increase in porosity values when the CNC dosage was increased above 1.00%. The porosity of the AA samples is higher than the OPC samples. The porosity of sealed cured AA samples increases when the CNC dosage was increased above 0.30%. This phenomenon can be attributed to the increasing "liquid/binder" of AA mixtures [43]. With the increase of CNC content in the AA samples, the "liquid/binder" ratio increases which leads to higher porosity of the samples. For heat-cured AA samples, the porosity slightly decreases with the addition of CNC. These results are consistent with the findings from the compressive strength measurements. As shown in Figure 10b, there is a strong linear correlation between the porosity and compressive strength results (compressive strength increases with the decrease of matrix porosity).

The measured electrical resistivity of the 3D printed samples as a function of CNC dosage is shown in Figure 11. There is no significant change in the electrical resistivity of OPC samples with the addition of the different dosages of CNC. The AA samples have significantly higher electrical resistivity compared to OPC samples. However, the AA samples showed a decrease in electrical resistivity with the increase in CNC content. For heat-cured AA samples, the electrical resistivity decreased slightly compared to that of sealed-cured samples. As stated, electrical resistivity is a fundamental property of a cementitious material that indirectly measures the resistance of microstructure against fluid penetration [20]. It should be noted that both OPC and AA samples were oven-dried and then vacuum-saturated with calcium hydroxide solution to eliminate the impact of pore solution composition (i.e., pore solution resistivity) on the measured electrical resistivity. However, it seems that the alkali leaching from reacted/unreacted products into the pore

solution of AA systems impacts the measured electrical resistivity. Further research is required to understand this phenomenon.

To further compare the resistance of AA and OPC samples against fluid penetration, the water absorption rate in OPC and AA samples with 1.00% CNC content was measured. The measured initial absorption of OPC-1.00% CNC (28-day wet-cured), AA-1.00% CNC (28-day sealed-cured), and AA-1.00% CNC (7-day heat-cured) samples are 4.68%, 7.64%, and 5.40% respectively. For AA systems, the initial absorption rate of heat-cured samples is lower than sealed-cured samples and comparable to the OPC system, which is in agreement with porosity measurements. It should be noted that the higher absorption rate in AA samples can partially be attributed to their higher "liquid/binder" when compared to the OPC samples.

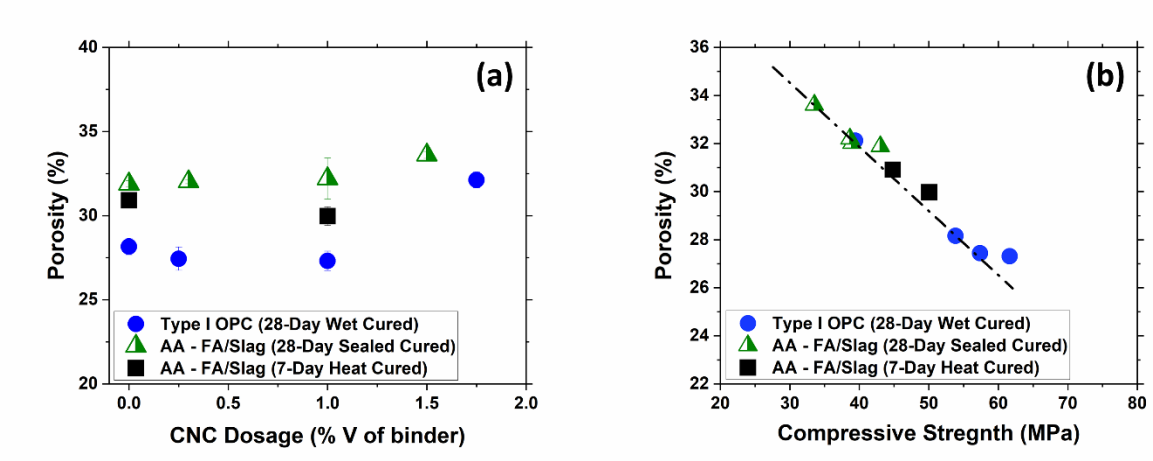

Figure 10. (a) Porosity of 3D printed OPC and AA samples with different dosages of CNC materials, and (b) porosity versus compressive strength for 3D printed OPC and AA samples.

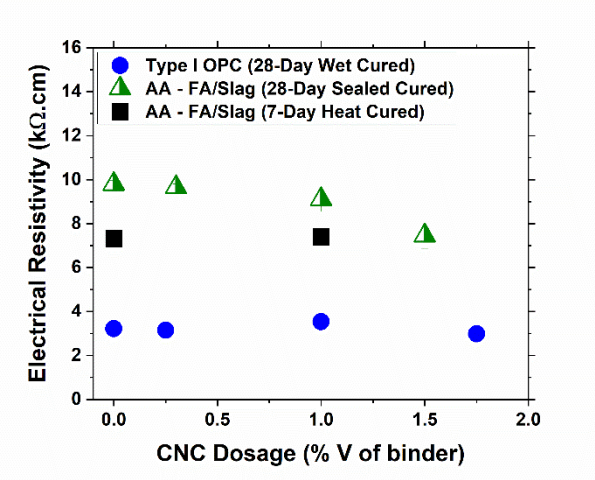

Figure 11. Electrical resistivity of 3D printed OPC and AA samples with different dosages of CNC materials.

6.4 Chemically Bound Water/Hydroxyls from TGA

Figure 12 shows the calculated total mass loss due to the decomposition of chemically bound water and hydroxyl ions from reaction products by TGA (i.e., mass loss between 50 °C and 580 °C divided by the mass of the binder) for OPC and AA samples as a function of the CNC dosage. Based on the results, the OPC–CNC samples have higher chemically bound water content, suggesting that the addition of CNC improves the microstructure. It should be noted that the increase of bound water content in the OPC mixtures with 1.50-1.75% CNC is partially related to the availability of extra water for reaction (due to higher w/c). Additionally, the increase of DOH due to CNC addition was reported in previous studies for conventional cementitious materials [13]. This increase can be explained by two different mechanisms: steric stabilization from CNCs which increases the desperation of binder particles, and the short circuit diffusion in which the CNCs adsorbed on the surface of binder particles and transport water from the capillary pores to the unhydrated cement or unreacted binder [13]. For AA samples, the inclusion of CNC does not have a significant impact on the amount of chemically bound water/hydroxyl ions.

Figure 13a shows the representative TGA weight loss and derivative thermogravimetry (DTG) curves illustrating the impact of CNC inclusion in the OPC system. It is evident from the graph that CNC increases the overall decomposition intensity of all the reaction products. Figure 13b shows AA - 1.00% CNC samples illustrating the decomposition intensity of ettringite, stratlingite, aluminosilicate gels (e.g., C-A-S-H, N-A-S-H or C-N-A-S-H), gibbsite, and calcium carbonate. The trend of both the sealed-cured and heat-cured AA samples is similar.

Figure 14 presents the calculated mass loss profiles (from chemically bound water/hydroxyl ions) of 3D printed OPC and AA samples over height after 28 days of wet curing or sealed curing for OPC and AA samples, respectively. Based on Figure 14, the OPC sample with 0.25% CNC has a higher amount of chemically bound water, especially at inner depths (CNC samples approximately show a 25% increase in DOH). This can be attributed to the internal curing potential of CNC materials. This is beneficial in low w/c systems such as 3D printed elements where the permeability of the matrix is low and the impact of external curing is limited to the surface layer [21, 44]. As shown in Figure 14b, the impact of external curing in OPC - Control samples (without CNC) is limited to the top 15 mm from the surface. On the other hand, the inclusion of CNC in AA samples does not have a significant impact on chemically bound water and hydroxyl ions content over the sample width.

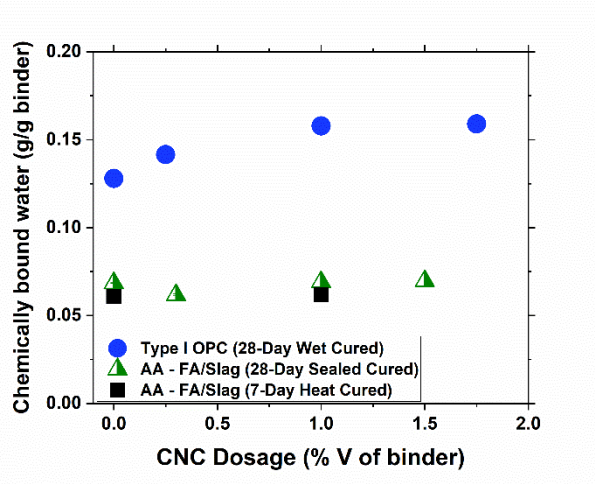

Figure 12. Chemically bound water and hydroxyl ions content as a function of CNC dosage in 3D printed OPC and AA samples

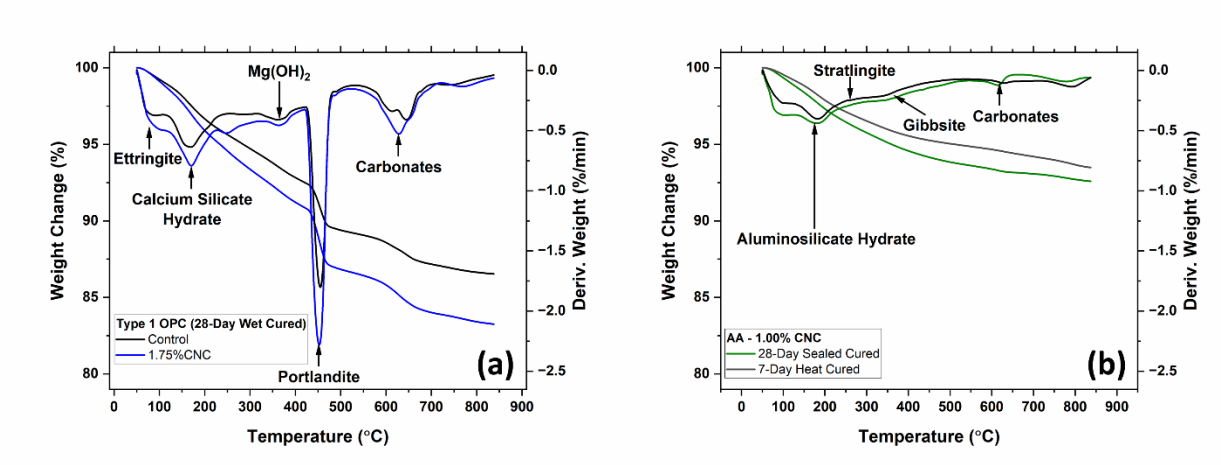

Figure 13. Representative TGA weight loss and DTG profiles of (a) OPC illustrating the impact of CNC and (b) AA - 1.00% CNC samples illustrating the impact of curing on the reaction products.

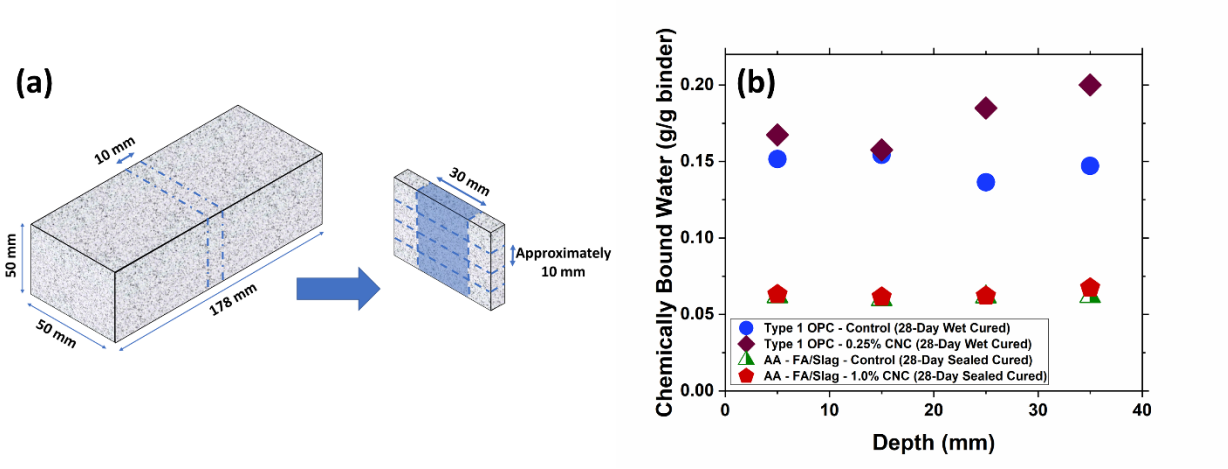

Figure 14. (a) Preparation of slices over the width of the 3D printed sample for TGA measurements and (b) chemically bound water and hydroxyl ions content profiles of 3D printed samples with and without CNC materials after 28 days of curing.

6.5 X-Ray Diffraction (XRD)

Figure 15 shows the X-ray diffraction patterns of 3D printed AA – Control and AA – 1.00% CNC both 28-day sealed-cured and 7-day heat-cured samples. X-ray diffraction patterns of raw FA and GGBFS powder are also shown. Based on Figure 15, the amorphous phases present in FA and GGBFS are indicated by a broad hump in the XRD spectrum [45, 46]. It is noticeable that GGBFS has two distinctive humps at approximately 10º-20º 2θ and 26º-35º 2θ with negligible crystalline phases, whereas FA has only one hump at approximately 10º-18º 2θ with some considerable crystalline phases of mullite, hematite, and quartz.

In Figure 15, the X-ray diffraction patterns of AA – Control and AA – 1.00% CNC both 28-day sealed-cured and 7-day heat-cured samples were magnified 15× compared to the raw FA and GGBFS XRD patterns to show the reflections in diffraction patterns. It is interesting that no amorphous humps were present in the sealed/heat-cured AA samples (between 10º and 35º 2θ). It indicates that most of the amorphous phases present in raw FA and GGBFS were consumed in alkali/hydration reactions and turned into crystalline and amorphous reaction products. The main

crystalline phases present in sealed/heat-cured AA samples are mullite, hematite, quartz, calcite, and anorthite. Compared with raw FA and GGBFS, the intensity of mullite (25.986º 2θ) and quartz (26.600º 2θ) phases in printed samples increased slightly. There is no significant difference between the heat- and sealed-cured samples except for the slight decrease in the intensity of mullite and quartz phases in heat-cured samples. Also, a decrease in the intensity of mullite and quartz phases is observed in AA samples with the addition of CNC. For amorphous phases, aluminosilicate hydrate gels such as N-A-S-H, C-A-S-H, and C-N-A-S-H are not crystalline and cannot be captured in XRD. This has been discussed in detail in Section 6.6.

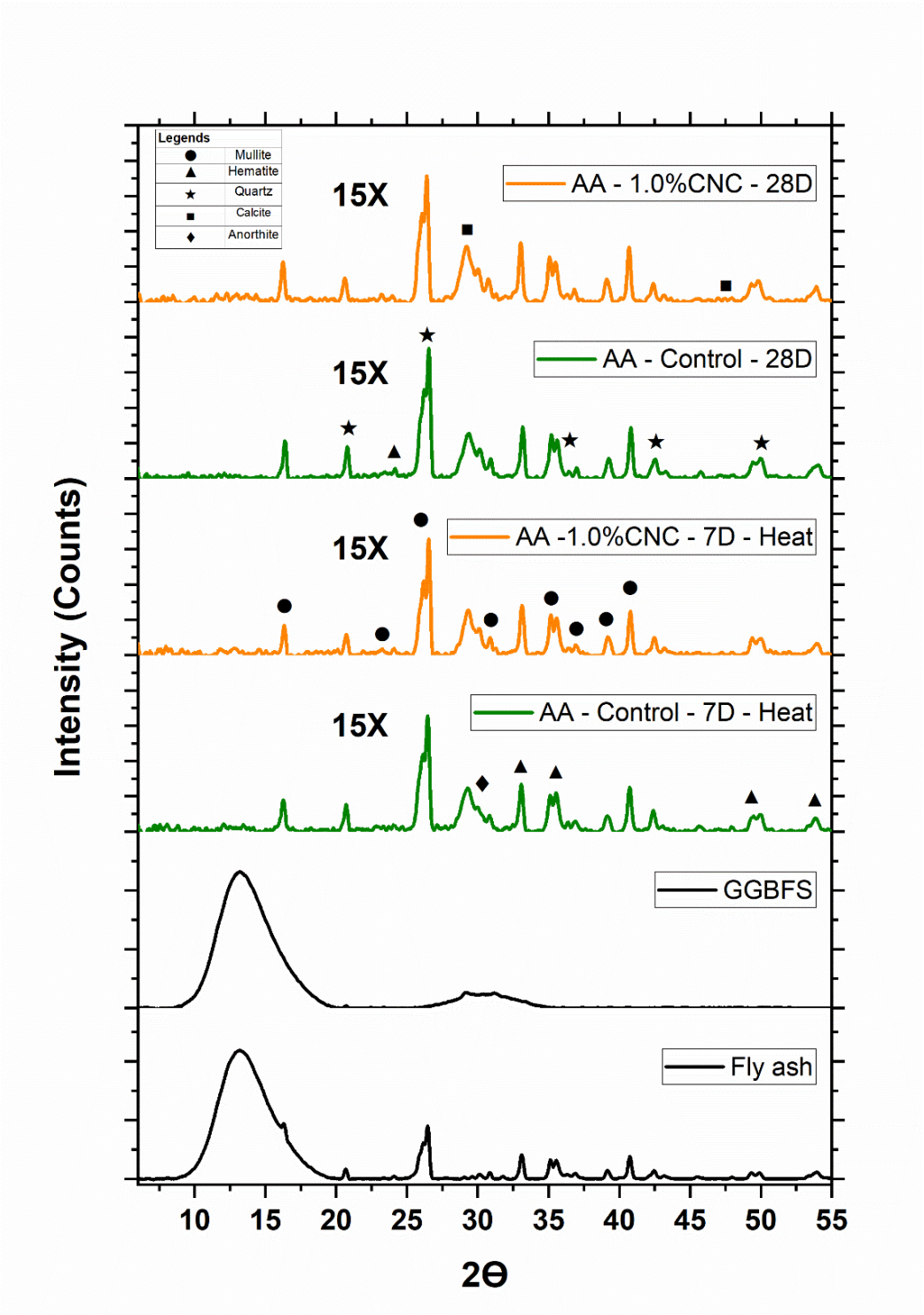

Figure 15. Comparison of x-ray diffraction patterns of raw FA and GGBFS with 3D printed AA samples with/without CNC.

6.6 Scanning Electron Microscopy (SEM) And Energy-Dispersive Spectroscopy (EDX)

The SEM micrographs of 3D printed AA – Control and AA – 1.00% CNC for both 28-day sealed-cured and 7-day heat-cured samples after flexural testing are shown in Figure 16. It is visible from the micrographs that the sealed-cured samples have a significantly higher amount of microcracks due to flexural stresses compared to heat-cured samples in the matrix. This is in an agreement with the lower flexural and compressive strength of sealed-cured samples compared to the heat-cured ones. Based on SEM micrographs, the FA particles in heat-cured samples are covered in gel-like reaction products which indicates that heat-curing increases the dissolution of unreacted particles of alkali-activated systems, and densifies the microstructure and interconnects the FA particles. In heat-cured samples, the FA particles are well embedded and connected to the matrix. The amount of unreacted FA particles is comparatively lower in heat-cured samples. The high porosity of the matrix and lack of connection between unreacted/poorly reacted FA particles are the main reasons for the low strength of sealed-cured AA samples. It is worth noting that the addition of CNC (up to 0.30% of the volume of the binder) in sealed-cured samples improves the flexural strength of the AA samples. This can be attributed to the crack-bridging mechanism of CNCs.

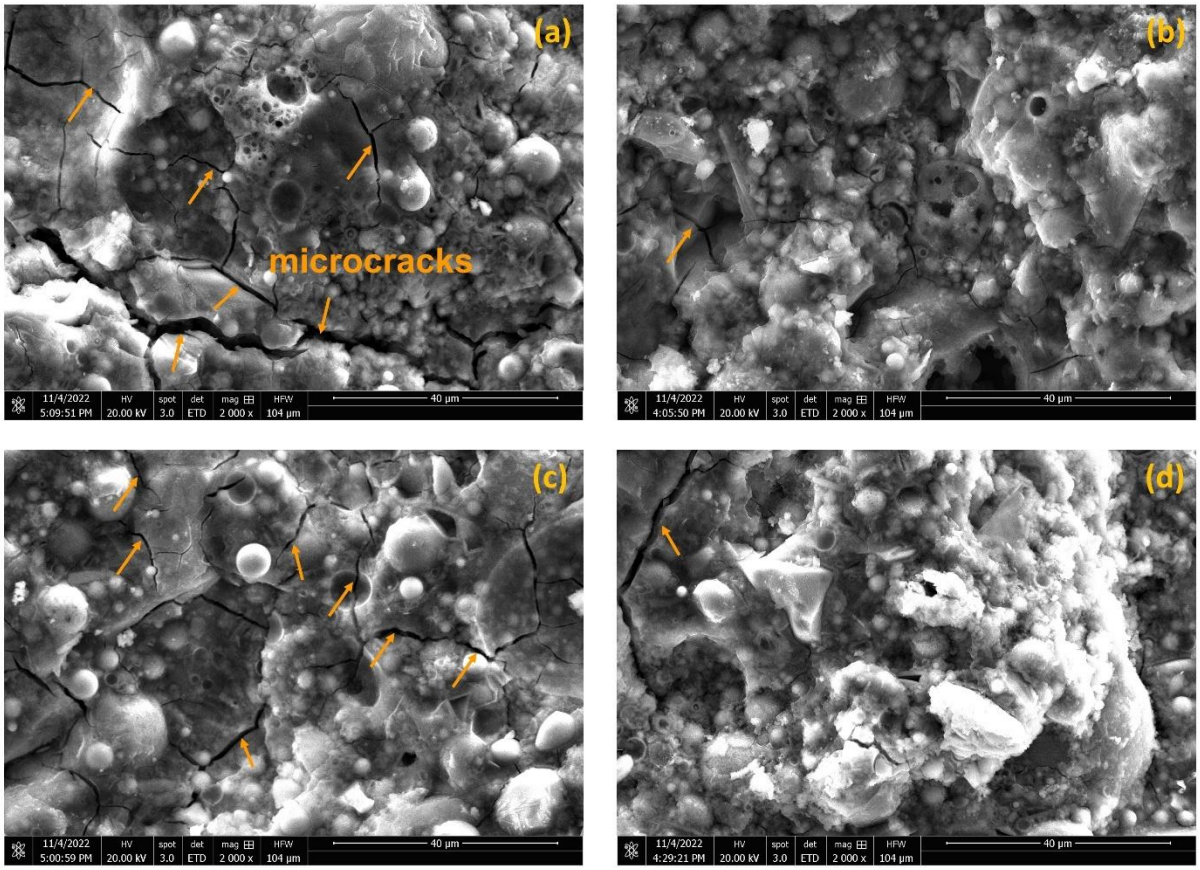

Figure 16. SEM micrographs of 3D printed AA – Control (a) 28-day sealed cured, (b) 7-day heat-cured samples and AA – 1.00% CNC (c) 28-day sealed cured, (d) 7-day heat-cured samples.

Further, energy-dispersive X-ray spectroscopy (EDX) was applied to characterize the elemental composition of alkali-activated products. Figure 17 shows the SEM micrographs of 3D printed AA-Control for both sealed-cured and heat-cured samples with identified reaction products and unreacted FA and GGBFS particles from EDX. Additionally, Table 4 provides the range of different elemental ratios (Na/Si, Na/Al, Al/Si, Si/Al, and Ca/Si) detected in the EDX analysis of 3D-printed AA samples of Figure 17. Based on EDX analysis, 28-day sealed cured samples show a higher amount of unreacted fly ash spheres. It is evident from the EDX analysis that aluminosilicate hydrate gels such as non-crosslinked N-A-S-H and C-A-S-H or crosslinked C-N-

A-S-H (with Na/Si of 0.39-0.6 and Si/Al of 1.80-2.17) are the main reaction product of AA systems. Bakharev [47] reported similar Si/Al ratios between 1.8 and 3.6 for a Class F fly ash activated by a sodium silicate activator. Gebregziabiher et al. [48] reported similar Ca/Si and Al/Si ratios of 1.12 and 0.37 for GGBFS activated by a 5 M sodium hydroxide activator.

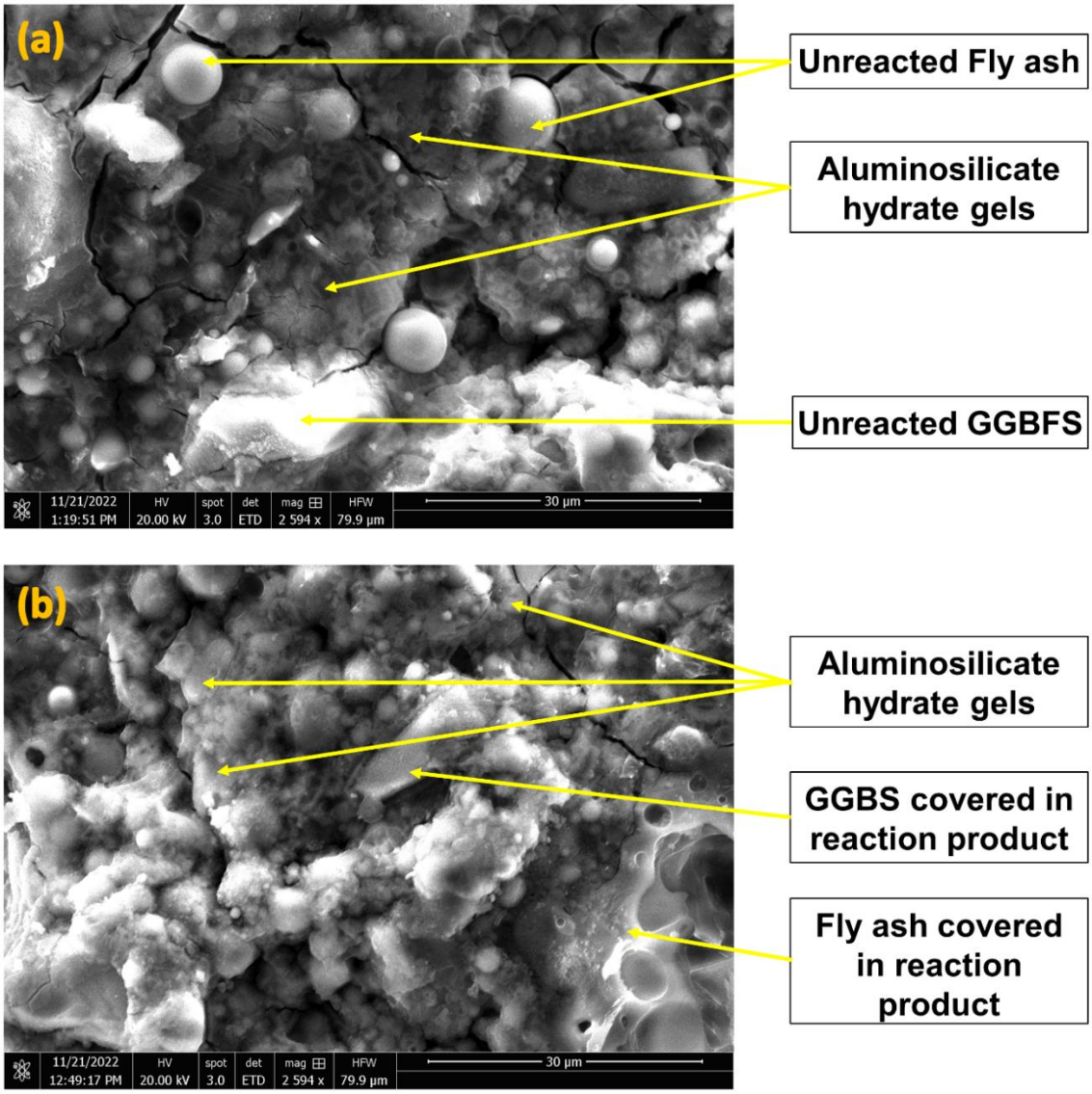

Figure 17. SEM micrographs with identified reaction products and unreacted particles of 3D printed AA – Control: (a) 28-day sealed cured, and (b) 7-day heat-cured samples.

Table 4
Range of different elemental ratios from EDX analysis

Region	Na/Si	Na/Al	Al/Si	Si/Al	Ca/Si
Aluminosilicate Hydrate	0.39-0.60	0.77-1.18	0.46-0.56	1.80-2.17	0.65-1.12
Unreacted FA	0.06-0.09	0.06-0.14	0.61-0.99	0.99-1.62	0.04-0.08
Unreacted GGBFS	0.16-0.20	0.33-0.44	0.44-0.49	2.05-2.25	1.31-1.64
Fly ash covered in reaction products	0.19-0.37	0.21-0.63	0.59-0.84	1.17-1.72	0.21-0.65
GGBFS covered in reaction products	0.19-0.36	0.28-0.94	0.36-0.60	1.62-2.71	1.20-1.33

CHAPTER 7
CONCLUSION

This study investigated the application of cellulose nanocrystals (CNC) in 3D-printed cementitious composites. Two different cementitious systems (OPC and alkali-activated (AA) mixtures) with varying dosages of CNC were examined. The AA mixtures were prepared with a combination of Class F fly ash (FA) and ground granulated blast furnace slag (GGBFS) as the precursor. A suite of experimental methods was applied to study the impact of CNC on the fresh and hardened properties of 3D printed mixtures.

To design extrudable CNC mixtures, the demand for the activator (i.e., "activator/binder") was increased linearly as a function of CNC dosage in AA mixtures. However, OPC mixtures required a more dramatic increase of the "liquid/binder" ratio above 1.0% CNC concentration in order to be extrudable. The buildability of the AA mixtures was improved by increasing the dosage of CNC, suggesting that the CNC performs as a viscosity-modifying agent in AA mixtures. The alkali-activated mixture with a "$NaOH/Na_2SiO_3$" mass ratio of "85/15" as the activator and a "FA/GGBFS" mass ratio of "70/30" as the precursor was selected as the optimum mixture for 3D printing.

The addition of CNC up to 1.00% increased the compressive strength and modulus of rupture (MoR) of the OPC mixtures, suggesting that the 1.00% CNC dosage is the critical concentration for CNC agglomeration in the studied OPC mixtures. The CNC agglomeration regions (in mixtures with CNC concentration higher than the critical dosage) can act as weak points in the microstructure of cementitious systems, and consequently reduce the mechanical performance of the 3D printed samples. The sealed-cured AA samples have a lower compressive strength

compared to OPC systems and it further decreased with the addition of a higher CNC dosage. However, their MoR values are comparable to OPC samples for up to 0.30% addition of CNC. Heat curing of CNC-incorporated AA samples at 60 ℃ positively impacted the mechanical performance of the AA samples. The heat-cured AA samples showed higher flexural strength than the OPC samples. Also, there is a strong linear correlation between the porosity and compressive strength results of both OPC and AA mixtures (compressive strength linearly increased with the decrease of matrix porosity).

For AA systems, the initial water absorption rate of heat-cured AAM samples is lower than the sealed-cured AAM samples and comparable to the OPC system. Despite the negligible impact of CNC on the electrical resistivity of OPC samples, the alkali-activated samples showed a decrease in electrical resistivity with the increase in CNC content. Additionally, the AA samples had higher electrical resistivity compared to the OPC samples. The higher electrical resistivity of AA samples can be attributed to the alkali leaching from reacted/unreacted products into the pore solution of AAM systems.

The inclusion of CNC showed greater chemically bound water content for OPC samples, suggesting that the addition of CNC (below critical concentration) improves the microstructure. The addition of CNC in OPC significantly increased the chemically bound water in the inner depths of the printed samples. This can be attributed to the internal curing potential of CNC materials. This is beneficial in low water-to-binder systems such as 3D-printed elements where the permeability of the matrix is low and the impact of external curing is limited to the surface layer. However, the inclusion of CNC in AA samples does not have a significant impact on the amount of chemically bound water/hydroxyls.

The main crystalline phases present in AA samples were mullite, hematite, quartz, calcite, and anorthite. The amorphous phases and part of the crystalline phases present in raw fly ash and slag were consumed by the reaction with the activator and water to primarily produce amorphous/crystalline reaction products. Further, the addition of CNC slightly decreased the intensity of mullite and quartz phases in CNC samples.

SEM micrographs confirm that heat curing increases the reaction of AA samples by increasing the dissolution rate of FA and GGBFS particles in alkali-activated systems. The FA particles in heat-cured samples are covered in gel-like reaction products. These reaction products densify the microstructure and interconnect the FA particles. In addition, microcracks due to flexural stresses in heat-cured samples are comparatively less than in sealed-cured samples. It is worth noting that the addition of CNC (up to 0.30% of the volume of the binder) in sealed-cured samples improved the flexural strength of the AAM samples. The EDX analysis confirms that the main reaction product of AA systems is aluminosilicate hydrate gels such as non-crosslinked N-A-S-H and C-A-S-H or crosslinked C-N-A-S-H (with Na/Si of 0.39-0.6 and Si/Al of 1.80-2.17).

The developed printable “alkali-activated-CNC” composites can provide an overall reduction in the environmental impacts of the 3D-printed cementitious composites by eliminating/reducing the need for different chemical admixtures (e.g., viscosity modifying agents) to improve 3D-printed material consistency and stability, and replacing 100% of portland cement with fly ash and slag.

REFERENCES

[1] A.R. Krishnaraja, K.V. Guru, 3D Printing Concrete: A Review, IOP Conference Series: Materials Science and Engineering 1055(1) (2021) 012033.

[2] R.J. Moon, G.T. Schueneman, J. Simonsen, Overview of Cellulose Nanomaterials, Their Capabilities and Applications, JOM 68(9) (2016) 2383-2394.

[3] A. Alsalman, L.N. Assi, R.S. Kareem, K. Carter, P. Ziehl, Energy and CO2 emission assessments of alkali-activated concrete and Ordinary Portland Cement concrete: A comparative analysis of different grades of concrete, Cleaner Environmental Systems 3 (2021).

[4] M. Amran, H.S. Abdelgader, A.M. Onaizi, R. Fediuk, T. Ozbakkaloglu, R.S.M. Rashid, G. Murali, 3D-printable alkali-activated concretes for building applications: A critical review, Construction and Building Materials 319 (2022).

[5] B. Nematollahi, M. Xia, P. Vijay, J.G. Sanjayan, Properties of Extrusion-Based 3D Printable Geopolymers for Digital Construction Applications, 3D concrete printing technology : (2019) 371.

[6] B. Nematollahi, P. Vijay, J. Sanjayan, A. Nazari, M. Xia, V.N. Nerella, V. Mechtcherine, Effect of Polypropylene Fibre Addition on Properties of Geopolymers Made by 3D Printing for Digital Construction, Materials 11(12) (2018).

[7] Z. Malaeb, F. AlSakka, F. Hamzeh, 3D Concrete Printing, 3D concrete printing technology : (2019) 115.

[8] T. Marchment, J.G. Sanjayan, B. Nematollahi, M. Xia, Interlayer Strength of 3D Printed Concrete, 3D concrete printing technology : (2019) 241.

[9] Y. Chen, S. He, Y. Zhang, Z. Wan, O. Copuroglu, E. Schlangen, 3D printing of calcined clay-limestone-based cementitious materials, Cement and Concrete Research 149 (2021).

[10] C. Zhang, V.N. Nerella, A. Krishna, S. Wang, Y. Zhang, V. Mechtcherine, N. Banthia, Mix design concepts for 3D printable concrete: A review, Cement and Concrete Composites 122 (2021) 104155.

[11] Y. Valadez-Carranza, C. Wilson, M.K. Moradllo, W.J. Weiss, Examining the effect of Cellulose Nanocrystals (CNC) on 3-D Printed Cement Composites, TRB 1st International Conference on 3D printing and Transportation, Washington DC, 2019.

[12] I. Garcia-Lodeiro, A. Palomo, A. Fernández-Jiménez, An overview of the chemistry of alkali-activated cement-based binders, Handbook of alkali-activated cements, mortars and concretes / (2015) 19.

[13] Y. Cao, P. Zavaterri, J. Youngblood, R. Moon, J. Weiss, The influence of cellulose nanocrystal additions on the performance of cement paste, Cement & Concrete Composites 56 (2015) 73-83.

[14] J.H. Aquino Rocha, L.d.N. Farias, T.P.L. Siqueira, Cellulose nanofibers (CNF) as reinforcement for cementitious matrices: a systematic literature review, Revista ALCONPAT 12(3) (2022) 311 - 327.

[15] Y.Z. Cao, N.N. Tian, D. Bahr, P.D. Zavattieri, J. Youngblood, R.J. Moon, J. Weiss, The influence of cellulose nanocrystals on the microstructure of cement paste, Cement & Concrete Composites 74 (2016) 164-173.

[16] M.E.-B. Jose Goncalves, Yaman Boluk, Vivek Bindiganavile, Cellulose nanofibres (CNF) for sulphate resistance in cement based systems, Cement and Concrete Composites 99 (2019) 100-111.

[17] Y.Z. Cao, P. Zavattieri, J. Youngblood, R. Moon, J. Weiss, The relationship between cellulose nanocrystal dispersion and strength, Construction and Building Materials 119 (2016) 71-79.

[18] N. Corporation, Cellulose Nanocrystals (CNC). https://www.novarials-store.com/products/copy-of-cellulose-nanocrystals-cnc.

[19] N. Corporation, Cellulose Nanofibers (CNF). https://www.novarials-store.com/products/cellulose-nanofiber-slurry-100ml-3g.

[20] H.H. Kolour, W. Ashraf, E.N. Landis, Hydration and Early Age Properties of Cement Pastes Modified with Cellulose Nanofibrils, Transportation Research Record 2675(9) (2021) 38-46.

[21] F. Montes, T.F. Fu, J.P. Youngblood, J. Weiss, Rheological impact of using cellulose nanocrystals (CNC) in cement pastes, Construction and Building Materials 235 (2020).

[22] X. Sun, Q. Wu, S. Lee, Y. Qing, Y. Wu, Cellulose Nanofibers as a Modifier for Rheology, Curing and Mechanical Performance of Oil Well Cement, Scientific Reports 6 (2016).

[23] A.G. Wang, Y. Zheng, Z.H. Zhang, K.W. Liu, Y. Li, L. Shi, D.S. Sun, The Durability of Alkali-Activated Materials in Comparison with Ordinary Portland Cements and Concretes: A Review, Engineering 6(6) (2020) 695-706.

[24] J.L. Provis, Alkali-activated materials, Cement and Concrete Research 114 (2018) 40.

[25] A.F. Jiménez, V.P. Krivenko, A. Palomo, Classification and Characteristics of Alkali-Activated Cements, Journal of the Chinese Ceramic Society 40(1) (2012) 7.

[26] A. Fernández-Jiménez, J.Y. Pastor, A. Martín, A. Palomo, High-Temperature Resistance in Alkali-Activated Cement, Journal of the American Ceramic Society 93(10) (2010) 3411-3417.

[27] L. Srinivasamurthy, V.S. Chevali, Z.H. Zhang, M.A. Longhi, T.W. Loh, H. Wang, Mechanical property and microstructure development in alkali activated fly ash slag blends due to efflorescence, Construction and Building Materials 332 (2022).

[28] M. Criado, W. Aperador, I. Sobrados, Microstructural and Mechanical Properties of Alkali Activated Colombian Raw Materials, Materials 9(3) (2016).

[29] M. Amran, R. Fediuk, H.S. Abdelgader, G. Murali, T. Ozbakkaloglu, Y.H. Lee, Y.Y. Lee, Fiber-reinforced alkali-activated concrete: A review, Journal of Building Engineering 45 (2022) 103638.

[30] Y.N. Chen, L.T. Jia, C. Liu, Z.D. Zhang, L. Ma, C. Chen, N. Banthia, Y.M. Zhang, Mechanical anisotropy evolution of 3D-printed alkali-activated materials with different GGBFS/FA combinations, Journal of Building Engineering 50 (2022).

[31] M. Chougan, S.H. Ghaffar, B. Nematollahi, P. Sikora, T. Dorn, D. Stephan, A. Albar, M.J. Al-Kheetan, Effect of natural and calcined halloysite clay minerals as low-cost additives on the performance of 3D-printed alkali-activated materials, Materials & Design 223 (2022).

[32] P. Sikora, M. Chougan, K. Cuevas, M. Liebscher, V. Mechtcherine, S.H. Ghaffar, M. Liard, D. Lootens, P. Krivenko, M. Sanytsky, D. Stephan, The effects of nano- and micro-sized additives on 3D printable cementitious and alkali-activated composites: a review, Applied Nanoscience 12(4) (2022) 805-823.

[33] B. Panda, S.Q. Ruan, C. Unluer, M.J. Tan, Investigation of the properties of alkali-activated slag mixes involving the use of nanoclay and nucleation seeds for 3D printing, Composites Part B-Engineering 186 (2020).

[34] H. Alghamdi, S.A.O. Nair, N. Neithalath, Insights into material design, extrusion rheology, and properties of 3D-printable alkali-activated fly ash-based binders, Materials & Design 167 (2019).

[35] M. Chougan, S.H. Ghaffar, P. Sikora, S.Y. Chung, T. Rucinska, D. Stephan, A. Albar, M.R. Swash, Investigation of additive incorporation on rheological, microstructural and mechanical properties of 3D printable alkali-activated materials, Materials & Design 202 (2021).

[36] B.R. Zhu, J.L. Pan, B. Nematollahi, Z.X. Zhou, Y. Zhang, J. Sanjayan, Development of 3D printable engineered cementitious composites with ultra-high tensile ductility for digital construction, Materials & Design 181 (2019).

[37] Cellulose Nanocrystals (CNC) Product Specification Sheet, The University of Maine Process Development Center, https://umaine.edu/pdc/wp-content/uploads/sites/398/2016/03/Specs-CNC.pdf.

[38] Y. Bu, R. Spragg, W.J. Weiss, Comparison of the Pore Volume in Concrete as Determined Using ASTM C642 and Vacuum Saturation, Advances in Civil Engineering Materials 3(1) (2014) 308-315.

[39] N. Khalil, G. Aouad, K. El Cheikh, S. Remond, Use of calcium sulfoaluminate cements for setting control of 3D-printing mortars, Construction and Building Materials 157 (2017) 382-391.

[40] M. Kosson, L. Brown, F. Sanchez, Early-Age Performance of 3D Printed Carbon Nanofiber and Carbon Microfiber Cement Composites, Transportation Research Record 2674(2) (2020) 10-20.

[41] S. Marinković, J. Dragaš, Fly ash, Waste and supplementary cementitious materials in concrete, Elsevier2018, pp. 325-360.

[42] M.S. El-Feky, M. Kohail, A.M. El-Lair, M.I. Serag, Effect of microwave curing as compared with conventional regimes on the performance of alkali activated slag pastes, Construction and Building Materials 233 (2020).

[43] Y.Y. Kim, K.M. Lee, J.W. Bang, S.J. Kwon, Effect of W/C Ratio on Durability and Porosity in Cement Mortar with Constant Cement Amount, Advances in Materials Science and Engineering 2014 (2014).

[44] L. Bouchelil, R.M. Ghantous, G. Clark, M.N. Goodwin, W.J. Weiss, M.K. Moradllo, Quantifying Impact of Internally Cured Concrete on Duration of External Curing, ACI Materials Journal 119(5) (2022) 269-290.

[45] G. Singh, K.V.L. Subramanian, Quantitative XRD study of amorphous phase in alkali activated low calcium siliceous fly ash, Construction and Building Materials 124 (2016) 139-147.

[46] A. Matsuda, I. Maruyama, A. Meawad, S. Pareek, Y. Araki, Reaction, Phases, and Microstructure of Fly Ash-Based Alkali-Activated Materials, Journal of Advanced Concrete Technology 17(3) (2019) 93-101.

[47] T. Bakharev, Geopolymeric materials prepared using Class F fly ash and elevated temperature curing, Cement and concrete research 35(6) (2005) 1224-1232.

[48] B.S. Gebregziabiher, R. Thomas, S. Peethamparan, Very early-age reaction kinetics and microstructural development in alkali-activated slag, Cement and concrete composites 55 (2015) 91-102.